Hierarchical TiN nanostructured thin film electrode for highly stable PEM fuel cells

Andrea Perego[a,b] *, Giorgio Giuffredi*[a,b]*, Piero Mazzolini*[a]*, Massimo Colombo*[c]*, Rosaria Brescia*[c]*, Dinesh C. Sabarirajan*[d]*, Iryna V. Zenyuk*[d,f]*, Filippo Bossola*[e]*, Vladimiro Dal Santo*[e]*, Andrea Casalegno*[b] *and Fabio Di Fonzo*[a]**.*

a. Center for Nano Science and Technology @PoliMi, Istituto Italiano di Tecnologia, via G. Pascoli 70/3, 20133 Milano (IT).

b. Dipartimento di Energia, Politecnico di Milano, via Lambruschini 4, 20133 Milano (IT).

c. Department of Nanochemistry, Istituto Italiano di Tecnologia, via Morego 30, 16163 Genova, Italy.

d. Department of Mechanical Engineering, Tufts University, 200 Boston Ave., Medford MA.

e. CNR-Istituto di Scienze e Tecnologie Molecolari, Via Golgi 19, Milano 20133, Italy.

f. Department of Chemical and Biomolecular Engineering, University of California, Irvine, CA

*corresponding author: fabio.difonzo@iit.it

KEYWORDS: Fuel Cells, Non-carbon Pt support, Nanostructured TiN, Stability

ABSTRACT: Fuel cell is to date on the brink of large-scale commercialization. Still, long-term stability is of concern, especially in the automotive field, mainly due to the stability of the cathodic catalyst support. Carbonaceous materials, that to date are the state of the art, suffer from severe corrosion phenomena during discontinuous operation. As shown in various works in the literature, titanium nitride (TiN) has a metal-like conductivity with an outstanding chemical stability and makes a good candidate to replace carbon. In this contribution, we report about hierarchical nanostructured thin films of Titanium Nitride (HTNTF), as high stability support for the Pt catalyst. The HTNTF are grown by a one step, physical vapor deposition (PVD) process that exploits the plasma dynamics to fine tune the morphology. Activity towards the oxygen reduction reaction is assessed, and stability is evaluated according to DOE Accelerated Stress Test (AST) standard protocols, and the ECSA loss is registered to be around 7% with respect to the 40% goal. Moreover, a proof of concept MEA has been realized to demonstrate the applicability of our supports to the device scale. Despite further optimization is needed to achieve high performances, our results show the potential of a new class of thin-film electrodes with superior stability to overcome carbon corrosion limitations.

1. Introduction

Polymer electrolyte membrane fuel cell (PEMFC) technology is the main candidate for next generation energy conversion devices and the cornerstone of the power-to-gas strategy to store the excess energy produced by renewable, discontinuous sources. To date, commercial solutions are available for a wide range of applications, from stationary to the automotive field[1,2]. Nevertheless, in view of a widespread penetration of the electrified mobility, the competitiveness of fuel cell technology is hampered by the high material costs and low lifetime, with respect to the established internal combustion engines and the emerging batteries[2,3]. In particular, long-term stability is affected mainly by the corrosion of the C-based supports for Pt at the cathodic electrode. In fact, during non-steady state and off-normal operating conditions in the typical automotive cycle like (start up, shutdown and fuel starvation) the cathodic potential can increase up to 1.5 V [4,5] at which the kinetics of C oxidation becomes significant. Carbon corrosion in the proximity of the Pt nanoparticles inevitably leads to their detachment, lowering the electrode electrochemically active surface area (ECSA), and, in turn, hampering its performances and durability. Different carbon structures with high level of graphitization have been proposed in order to increase corrosion resistance, such as nanotubes[6,7], or graphene-based 2D structures[8–10]. Although these materials are more corrosion-tolerant than the standard carbon black, they still suffer from corrosion since they consist mainly of carbon. To overcome this long-term stability issue, recent studies focus on replacing carbon with other types of materials. Transition metal oxides (MOs) such as TiO_2 [11–14] and SnO_2[11,15] have been selected as good candidates for their stability, but they have limited electrical conductivity and need to be highly doped. Another solution is to use a carbon-MO composite to exploit the carbon part only as an electron carrier[11,16]. Even though in this configuration carbon does not act as a catalyst support, the electrodes still suffer from corrosion

issues under PEMFC operating conditions. In this scenario titanium nitride (TiN) has drawn attention in the past few years for its unique combination of metallic conductivity[17] and remarkable chemical inertness[18]. Its performances as a support for oxygen reduction reaction (ORR) catalyst as well as its stability at cathodic conditions[19–24] are evaluated in the literature: the higher binding strength with Pt grants better catalytic performance and stability[25] with respect to carbonaceous supports. Moreover, the it shows an intrinsic high corrosion resistance, that can be attributed to a native TiO_2/TiO_xN_y passivation layer which forms at the surface[18] preventing further oxidation of the bulk nitride core. This class of catalyst supports is generally fabricated in two steps: from the reduction of a titanium precursor, TiO_2 particles or more complex structures (e.g. nanotubes, nanofibers) are obtained, thus setting the morphology of the support[22]. This is followed by a first annealing in air and then by a nitridization step in pure ammonia atmosphere at temperatures higher than 800°C[21]. This fabrication routes are energy intensive and inevitably lead to particle sizes in the order of several tens of nanometers and little control on the pore size distribution. In fact, the typical specific surface area is below 39 $m^2\ g^{-1}$ except for the work by Kim et al[21] which showed a remarkable 181 $m^2\ g^{-1}$ with a pore size distribution below 10 nm. While these works confirmed the stability of the Pt/TiN system in the 0.5-1.1 V range (typical Pt dissolution AST) up to 10000 cycles, none of them reported tests in the 1-1.5 V range, typical of the AST for support corrosion given by the DOE[26,27]. Moreover, all the cited papers refer exclusively to electrodes fabricated by inks and tested on RRDE. In this work we move from the abovementioned literature and from the concept of nanostructured thin film (NSTF) electrode, as developed by 3M[28–32], to develop the first example of hierarchical TiN nanostructured thin film electrode (HTNTF), fabricated solely by room-temperature processing steps, active towards ORR and exhibiting excellent stability, with an ECSA loss of only 7% after 5000 cycles in the 1-1.5 V range (as DOE protocol for support

corrosion[26]) and of 13% after 15000 cycles. Moreover, we show how the HTNTF can be implemented in a membrane electrode assembly (MEA) through a custom decal process with promising performances.

2. Experimental

2.1 Fabrication of the catalyst

For the characterization in RRDE, the HTNTF is deposited directly on its tip and consequently Pt by means of pulsed electrodeposition technique. Glassy carbon rotating disk electrode (RDE) tips and glassy carbon disk/platinum ring rotating ring disk (RRDE) tips (Metrohm) were mirror-polished with sandpaper and alumina paste and subsequently sonicated in acetone and isopropanol (Honeywell). Electronic grade silicon (SiMat) and soda lime glass microscope slides were used as well for imaging and physical characterization. The nanostructured thin films were deposited via Pulsed Laser Deposition (PLD) technique by means of a KrF excimer laser (Coherent Gmbh. wavelength λ=280nm) using a 20Hz frequency and a fluence of 3.4 J cm^{-1} $pulse^{-1}$ ablating a TiN target (99.95%, Testbourne ltd.) in a vacuum chamber previously evacuated at 0.003 Pa, Deposition was performed in a N_2-H_2 (95%-5%) atmosphere. Different operation pressures (spacing from 15 to 100 Pa) were investigated with the aim of tuning the resulting thin film morphology. Number of pulses was adjusted to deposit a uniform, 1 µm thick film. For MEA application, thickness was increased to 5 µm. To load the support with metal catalyst, TiN-coated RDE tips were placed in a two-electrode electrochemical cell setup, with a Pt wire as a counter electrode and in a 0.5 M H_2SO_4 + 1 mM H_2PtCl_6 solution. Electrodeposition was performed using 50 ms cathodic current pulses of 50 mA cm^{-1} driven by Metrohm Autolab potentiostat (M204). 500 ms was chosen as the resting time between pulses. Rotation speed was set at 350 rpm to

remove the hydrogen bubbles forming during electrodeposition. The correct loading was determined by setting the correct number of pulses, given a target platinum loading of 300 μg cm^{-2}, while the current and on(off)-time signal was optimized with ECSA as figure of merit. Elemental analysis was performed on different values of the total charge to calibrate the correct platinum quantity that is deposited. Pt loadings were determined by Inductively-Coupled Plasma-Optical Spectroscopy (ICP-OES, ICAP 6200 Duo Upgrade, Thermo Fischer Scientific) after digestion of the samples in aqua regia.

2.2 Structural characterization

Morphology of the support and catalyst was evaluated by SEM imaging, using a ZEISS Supra 40 A. A micro Raman confocal microscope (inVia Raman Microscope Renishaw) using a 50x objective and an excitation wavelength of 785nm at 100 mW incident power was then used to check the fingerprint of TiN crystals and to assess the nitrogen content in the structure. Crystal properties were evaluated by grazing incidence XRD GI-XRD) analysis in a Bruker D8 Advance diffractometer with Cu Kα radiation (λ = 0.15418 nm), in the 30 to 90° range. Generator settings were 40 kV and 40 mA. XRD measurements were then confirmed by TEM imaging, together with EDS. The instrument used is a JEOL JEM-2200FS TEM operated at 200 kV, equipped with CEOS image aberration corrector, in-column image filter (Ω-type) and EDS spectrometer (Bruker, XFlash 5060 detector). The properties of the porous film were evaluated by gravimetric analysis: 8 cm diameter round aluminium foil were deposited with a fixed amount of material and weighted before and after the deposition. At the same time, the thickness profile was measured on samples deposited on Si (100) samples. With the radial symmetry of the film thickness, the volume could be estimated by integrating the profile on the radial coordinate, and density could be calculated

accordingly. Specific surface areas and pore sizes of the porous film were measured by nitrogen physisorption isotherms at -196 °C (77 K) using the using the BET method and BJH equations, outgassing the samples at 150 °C (423 K) for 2 h before each measurement.

2.3 Electrochemical characterization

Catalysts were tested in a room-temperature, three-electrode RDE glass cell (Pine instruments) in 0.5 M H_2SO_4 electrolytic solution. Ag/AgCl electrode was used as a reference while a Pt wire as counter. Cyclic voltammetry was performed to evaluate the electrochemical surface area (ECSA) of the Pt catalyst (potential sweep from 0.05 V to 1.4 V vs RHE at 0.15 V s^{-1}), while linear sweep voltammetry at different rotation speed (in the range between 600 to 2000 rpm) in 0.1M $HClO_4$ were performed to evaluate the ORR activity, sweeping the potential from 1 V to 0.2 V vs RHE in oxygen-saturated electrolyte solution. To assess the stability of the catalyst, an accelerated stress test was performed according to US DOE guidelines[26,33]: cyclic voltammetry was performed with a sweep from 1V to 1.5 V at 0.5 V s^{-1} for 5000 cycles. ECSA is evaluated with a CV cycle between 0.05 V and 0.6 V at 0.02 V s^{-1} in 0.5 M H_2SO_4 electrolytic solution at fixed cycles given by the DOE procedure. The threshold ECSA loss is 40%.

2.4 MEA fabrication and testing

To transfer the HTNTF electrode on the membrane, a modified decal process has been developed specifically for our material. This approach allowed to (i) separate the fabrication of the catalyst layer and the MEA, (ii) tuning the morphology and composition of the catalyst layer while (iii) allowing its transfer on the membrane afterwards. The process is represented in **Figure 7b**. The

HTN support is grown on a Si substrate coated with 100 nm sacrificial layer of MoO_x, grown by PLD in Ar atmosphere from a pure MoO_3 target (laser fluence: 3.1 J cm^{-1} $pulse^{-1}$, 15 Pa operating pressure). Atomic layer deposition (ALD) process is used to coat the TiN nanostructures with platinum, since electrodeposition is not feasible on insulating substrates. A Cambridge Nanotech Savannah Deposition ALD has been used for the deposition. ALD thermal exposure mode was used at 250 °C using trimethylcyclopentadienyl platinum (Me_3cpMePt) precursor for the metal and oxygen as a reducing agent. The single ALD cycle consists in pulsing the metal precursor and the oxygen respectively for 0.015 s and 5 s, with a purging step afterwards with pure nitrogen gas (99.9999%) to eliminate the residual and non-reacted precursors. The cycle is repeated to form a Pt layer to coat the HTNTF surface with a total loading of 0.360 mg cm^{-2}. To ensure ionic conductivity in the electrode, 0.01 mg cm^{-1} of liquid Nafion® dispersion (1%) was drop casted on the coated electrode before being pressed against Nafion® N212 membrane. For the purpose, a hot press was used, operated at 150°C for 5 minutes. Before peeling off the substrate, the assembly was immersed in 0.5 M sulfuric acid solution, to dissolve the sacrificial layer, so to obtain the complete transfer of a 1 cm^2 HTNTF catalyst layer. For the anode side, a Pt/C catalyst ink with a loading of 0.1 mg cm^{-2} was drop cast onto the gas diffusion layer (GDL), Sigracet 25BC and allowed to dry at a room temperature. The electrodes are then pressed between the anode gas diffusion electrode (GDE) and cathode GDL, also Sigracet 25 BC. Hard-stop fiberglass gaskets were used, resulting in a 25% compression. The MEA was tested in a 5 cm^2 cell hardware (Scribner Associates) with flow-rates of 200 ml min^{-1} and 300 ml min^{-1} for hydrogen and air at the anode and cathode sides, respectively. Relative humidity was kept at 90% for the reference measurements and at 50% for the dehydrated conditions. A back pressure of 100 kPa was used. Break-in of the cell with a cyclic procedure composed by 30 s potential step of 0.7, 0.5, 0.3 V until the current

values obtained were stable. Polarization curves were performed in a potentiostatic mode with 10 min potential holds. Electrochemical impedance spectroscopy (EIS) measurements were performed after every polarization point, in a 10000-0.1 Hz range with a 5% amplitude on the voltage signal. For cyclic voltammetry (CV) measurements, 100 ml min^{-1} of hydrogen and 100 ml min^{-1} of nitrogen (99.9999% purity) were fed to the cell, without back pressure. 25 mV min^{-1} scan rate was used for the analysis.

3. Results and discussion

The HTNTF is fabricated exploiting room-temperature, self-assembly of clusters from the gas phase produced in a supersonic plasma plume interacting with a background gas, in what we call a scattered ballistic deposition, SBD. The supersonic plasma plume can be generated by a laser ablating a solid target, this is the case of Pulsed Laser Deposition operated in SBD mode or PL-SBD[34–39] , or by a non-thermal low-pressure plasma jet in a continuous flow arrangement, LPPJ-SBD[40–42]. In this communication we choose to use PLD-SBD to its intrinsic higher simplicity, even if the production of TiN nanoparticles in powder form by low-pressure continuous flow reactors have been recently demonstrated[43,44]. In PL-SBD a crystalline TiN target is placed in a vacuum chamber in a nitrogen-5% hydrogen atmosphere and a pulsed excimer laser is focused on it generating a supersonic plasma plume which expands towards the substrates placed head-on[45]. When the background pressure is sufficiently high, the atomic and molecular species in the plume are scattered by the background gas, acquiring a velocity component in the plane perpendicular to the direction of motion and slow down. Part of the kinetic energy is spent to nucleate the physical vapours into small clusters which may or may not crystallize, depending on the energy available in the system. The clusters impinging on the substrate self-assemble into statistically regular arrays

of tree-like, hierarchical quasi-1D nanostructures due to a combination of random perpendicular velocity component and shadowing. PLD-SBD allows a precise control over film morphology from the nano to the micro-scale, since the internal structure of the trees and their spacing are governed by the deposition conditions[35,46]. Background gas pressure is the main control parameter of this process as shown in **Figure 1a**. The trend is the one already observed for titanium dioxide[35,47]: the film mesostructure evolves from columnar at 15 Pa to tree-like, with at an increase in porosity determined by the simultaneous growth in the branches opening and of the spacing among the trees, with a progressive loss of coherence as observed for the film deposited at 100 Pa, which shows aerogel-like features.

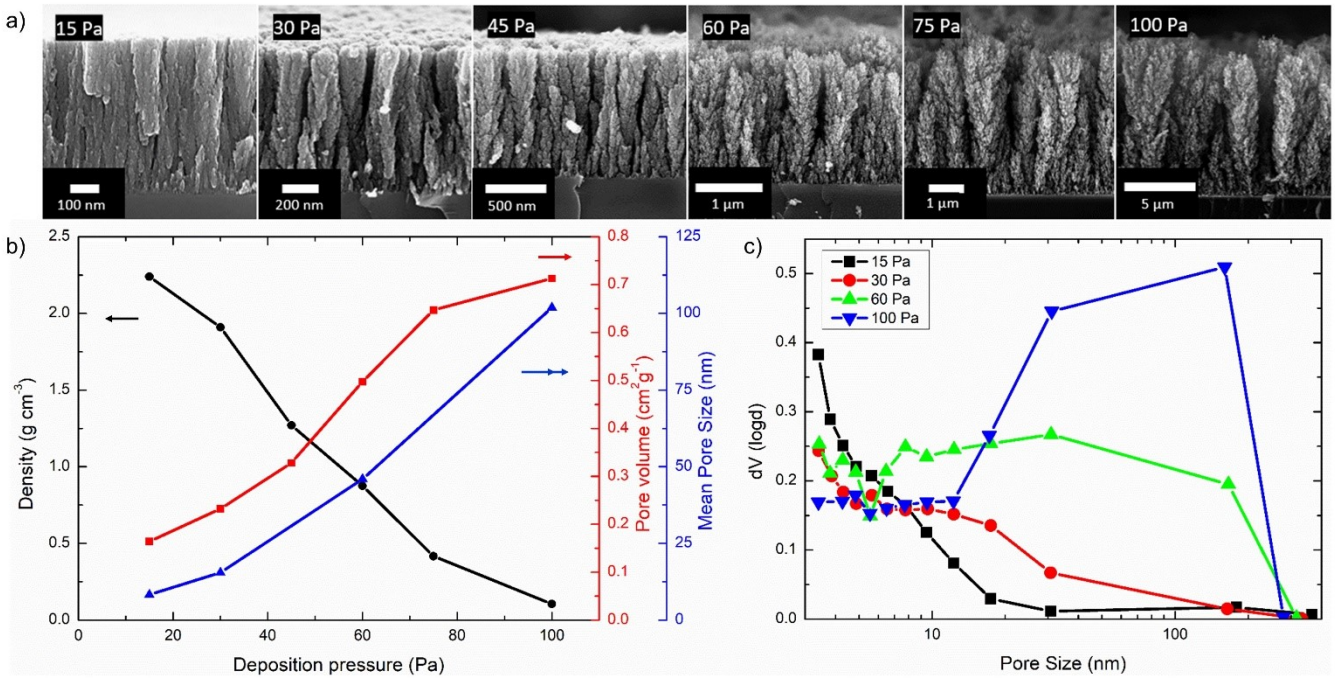

Figure 1. a) SEM images of the nanostructures obtained with different N_2-H_2 pressure at the same number of laser pulses. b) Density, pore volume and mean pore size dependency on the operating pressure of the HTNTF. c) Pore size distribution of films at different pressure from the nitrogen adsorption analysis.)

This evolution in mesostructure translates in a relevant increase in thickness growth rate, total pore volume and mean pore size with pressure and a decrease in density, down to 0.1 g cm^{-2} at 100 Pa, as shown in **Figure 1b**. We point out that, despite the just mentioned change in film properties, the BET surface area lays between 150 and 169 m^2 g^{-1} for all explored deposition conditions. We attribute this to the substantial shift towards larger size of the pore distribution with pressure, **Figure 1c**, which makes the BET analysis inaccurate and leads to an increasing underestimation of the contributions of large pores to the measured specific surface area. Nevertheless, the pore size distribution, obtained by the BHJ method, clearly demonstrate the evolution from the dense columnar structure with pores below 15 nm to a hierarchical structure with a uniform pore distribution up to 200 nm at 60 Pa. At 100 Pa the modal value of the pore size distribution shifts to values above 200 nm, and, correspondingly, the estimation of the surface area become unreliable. It is instructive to notice that the pore size distribution is a direct statistical quantification of the geometrical features of the HTNTF imaged by SEM. In fact, the looser packing of the TiN nanoparticle within each nanotree and larger spacing in between individual nanostructures going from a deposition pressure of 15 Pa to 60 Pa is quantitatively described by the reduction of the population of pores in the sub 10 nm pore size range, and a concomitant increase of the pore population between 10 and 200 nm. As an example, in the 60 Pa sample the fraction of pores larger than 100 nm refer to the spacing between the trees, while the smaller one to their inner structure. In the light of this preliminary study, a deposition pressure of 60 Pa was chosen as a trade-off between porosity and mechanical properties, **Figure 2a**. In fact, an ideal cathode for fuel cells must comply simultaneously to stringent requirements in terms of high electrical conductivity and mechanical stability, typical of high density films, and high surface area, facile ionomer infiltration and efficient mass transport, characteristics of the high-pressure

films. The HTNTF grown at 60 Pa exhibits a meso-range mean pore size (10-50 nm) which should be favourable to the accessibility of the sites by the reactants through the porous medium[48], but at the same time it has enough mechanical resistance to be handled in the electrochemical setup for electrodeposition and testing. The mean pore size is found to be 49.6 nm, while nitrogen adsorption measurements indicate a pore volume of 0.469 cm^3g^{-1} for pore volume and a BET area of 169 m^2g^{-1}, a value comparable to a graphitized carbon black support[49]. The large vertical channels in between the single nanostructures comprising the HTNTF are an almost ideal pathway for ionomer infiltration and gas access, considering that the mean free path for oxygen at ambient pressure is 68 nm.

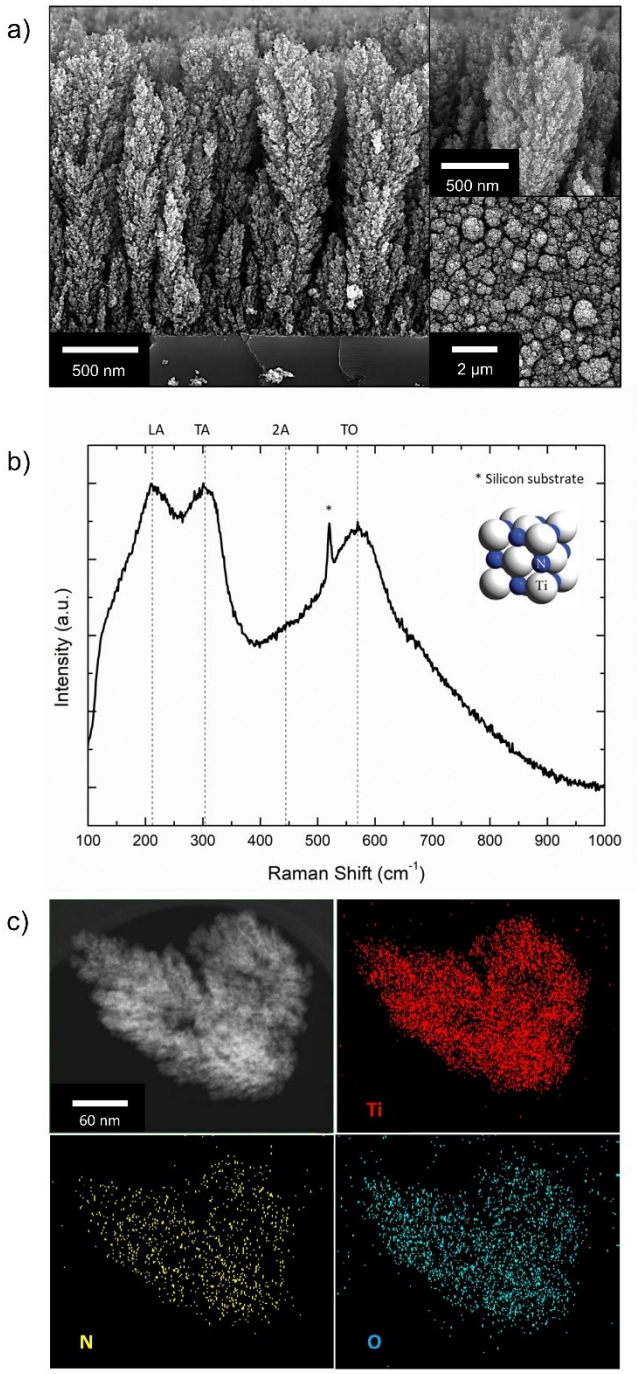

Figure 2. a) SEM image of the 60 Pa nanostructure, with details and the top view in the inset. b) Raman spectrum of the HTNTF with indication of the position of the vibrational modes from the literature[50] . c) EDS imaging of a portion of the HTNTF scratched from the film

3.1 Structural characterization of TiN support

Understanding the structure of the TiN nanotrees is crucial for the explanation of their behaviour as Pt support. Hence, we first investigated the grown HTNTFs by means of Raman and TEM. Due to the octahedral symmetry in perfect TiN cubic crystals, first order Raman scattering is forbidden[51]. Therefore, the detected Raman signal shown in **Figure 2b** is due to defect-driven first order scattering. The spectrum obtained is in line with other works presented in the literature about defective TiN lattices[50–53]. Nitrogen vacancies on the edges result in the increase of the mobility of the titanium on the vertex, enhancing the intensity of TA and LA vibrational modes in the cubic structure as observed in[54]. Therefore, Raman spectroscopy qualitatively suggests the presence of nitrogen vacancies in the scaffolds. Energy Dispersive X-ray Spectroscopy (EDS) mapping, **Figure 2c**, reveals the strong presence of oxygen, up to 35% (atomic). The reason for this contamination is attributed to the oxygen present in the atmosphere that saturates the nitrogen vacancies upon ventilation of the deposition chamber. Moreover, the low crystallinity and the high porosity of the films leave them open to oxidation also in the inner shell of the nanostructure. TEM, **Figure 3a**, indicates that the nanotrees comprising the HTNTF are formed by 7 nm crystals embedded in an amorphous matrix and the cell parameter was found to be 4.2 Å. A further confirmation of the TEM results is given by XRD spectra in **Figure 3b**, where the typical pattern of cubic TiN[55] is present. The shift towards higher angles and a low signal-to-noise ratio are attributed to low crystal size, 7-8 nm as calculated from the (200) and (220) peaks by the Scherrer equation, and to the presence of an amorphous fraction in the material.

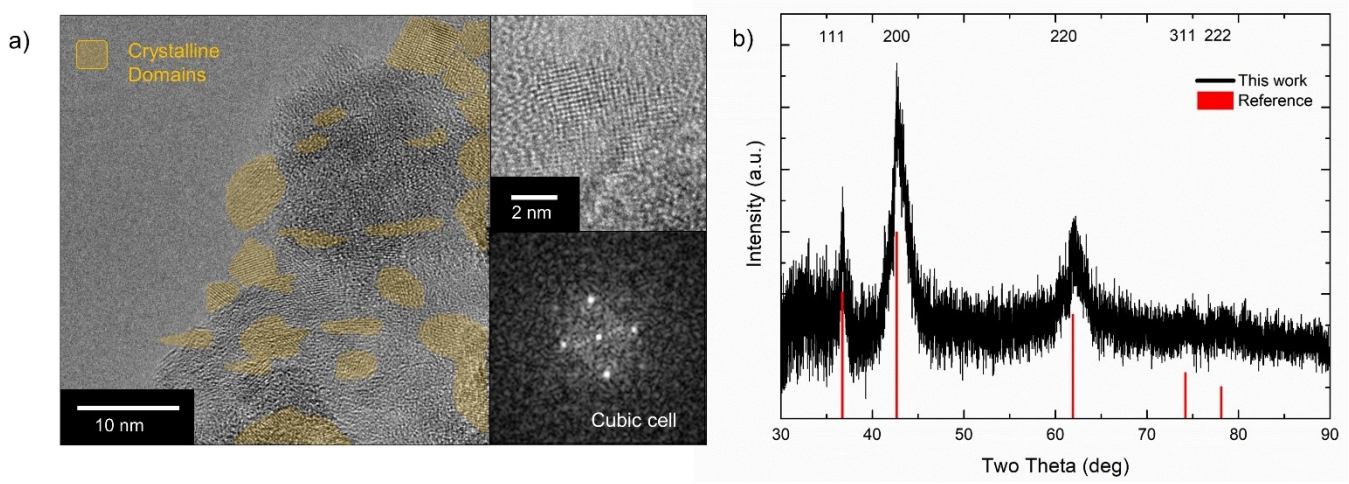

Figure 3. a) TEM image of a portion of HTNTF, showing the crystalline domains in the amorphous matrix. Details on the cubic domains and SAED electron diffraction pattern are shown in the inset. b) Raw XRD pattern HTNTF, compared to the literature reference53.

The cell parameter calculated from the XRD pattern is 4.21 Å, lower than the literature reference[55]. A possible explanation this phenomenon could be attributed to the nitrogen loss during the supersonic expansion of the plasma plume and the subsequent saturation of the vacancies with oxygen. The nitrogen deficiency in the TiN lattice can be calculated by the empirical formula[56–58] correlating the nitrogen content and a cubic cell parameter :

$$a = 0.4159 - 0.000164x$$

Where a is the cell parameter of the cubic structure and x the atomic N percentage. From our results, nitrogen content is decreased by 10-24%. In such scenario, it is possible that nitrogen vacancies are passivated with oxygen from atmospheric air: as reported in[59], oxidized TiN can be considered a solid solution of TiN and TiO, and therefore according to Vegard's Rule the lattice

parameter should lie between the reference material (4.235 Å) and the lattice parameter of cubic TiO (4.159 Å) .

3.2 Catalyst testing

Electrochemical surface area of the HTNTF electrode on RRDE was evaluated by integrating CV peaks between 0.05 V and 0.4V, corresponding to the hydrogen desorption from the crystal facets of the Pt as in[60]. The CV curve (**Figure 4a**) shows the usual features of a Pt catalyst in acid solution, with the hydrogen adsorption/desorption peaks at low potential, the onset of Pt oxidation at ~0.9 V and lastly, the Pt oxides reduction peak in the reverse scan at ~0.85 V. ECSA value is found to be 94.6 cm^2_{Pt} $cm^{-2}_{geom.}$ or 32.5 m^2 g^{-1}, considering the 0.3 mg_{Pt} cm^{-2} loading. Even though this value lies below the standard Pt/C commercial products (~60 m^2 g^{-1}), it is adequate in this study to assess the electrochemical performances and stability of the HTNTF electrode. SEM images of the electrodeposited sample are shown in **Figure 4b**. Platinum clusters self-assembled in rather unusual lamellar shape are visible on top of the nanotrees. This evidence may be the consequence of a non-uniform distribution of the charge on the scaffold: the irregular surface of the film presents sharp edges (as visible in the terminations of the nanotree "branches" in **Figure 2a**) where, due to the small radius electrons can be concentrated possibly resulting in a reaction rate enhancement.

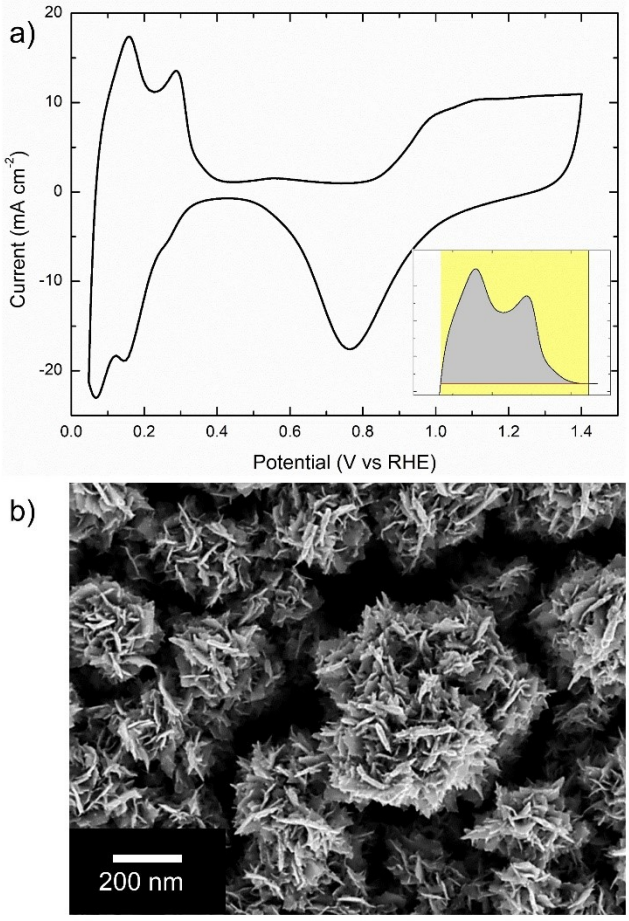

Figure 4. a) Cyclic voltammetry of the electrodeposited Pt/TiN in 0.5M H_2SO_4 solution, with a 150 mV s^{-1} scan rate. b) SEM top view of the electrodeposited Pt/TiN showing the lamellar structure of the metal

From XRD analysis we learn that the platinum lamellae (**Figure SI1**) have a mean size of crystal domains of 19 nm (as calculated by the Scherrer formula) and that a mean isotropic compressive strain of ≈ 1.1%[40,61,62] is present, as calculated by the positive Pt peak shift. Since the most relevant expected characteristics of the HTNTF scaffold is its high corrosion resistance and stability, standardized US-DOE accelerated degradation tests (see Section 2 for details) for the catalyst[26] and the support[63] were first performed. The support corrosion AST on Pt/TiN catalyst is shown in **Figure 5a.** Such procedure is meant to test the resistance of the catalyst support to the harsh environment that can be present during fuel cell operation for the automotive field, which has the

strictest stability requirements: potential is swept between 1 and 1.5 V, simulating the most aggressive conditions (e.g. in cases of fuel starvation, and in start/stop transients) in which a PEMFC cathode could work. Under those pH/potential conditions, the platinum stable phase is the oxidised one, so it does not take part in any reaction once it is completely oxidized (except during scans meant to measure the ECSA value, which are performed between 0.05 and 0.6 V). Hence, the only possible pathway for ECSA decrease is support corrosion with the consequent loss of electrode material. **Figure 5b** shows that the shape of the CV is substantially constant over the 5000 cycles of the test, and the final ECSA is as high as 7%. We performed other two subsequent identical AST protocols of 5000 cycles each to confirm the first outcome, and the results were similar, having a total loss of 13% after 15000 cycles. This result demonstrates the superior stability of the HTNTF as a cathodic catalyst support with respect to typical carbon-based catalytic inks[64].

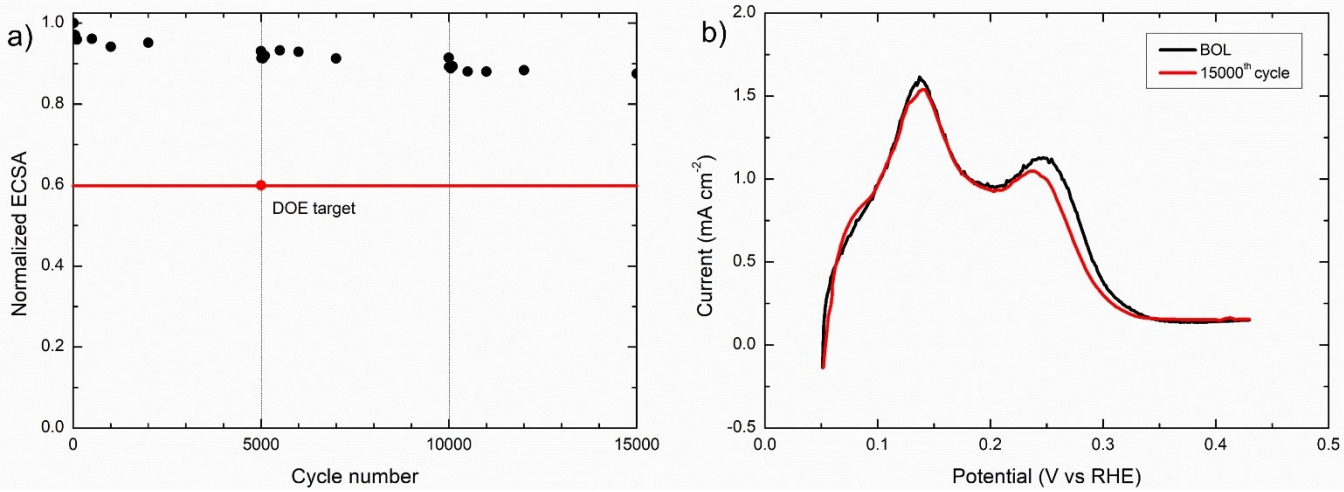

Figure 5 a) Normalized ECSA value monitored during the 15000 AST cycle for support corrosion performed on the RRDE setup between 1 and 1.5V vs RHE at 0.5 Vs^{-1} scan speed. Red line marks the DOE target for 5000 cycles. b) Comparison between the hydrogen desorption features at low potential of the cyclic voltammetry taken at the first cycle versus the 15000th cycle

From an activity point of view, the LSV curves, **Figure 6a**, indicate that the HTNTF electrode can reach good diffusive currents, comparable, if not better to commercial catalysts. This might be attributed to the different interface between the liquid phase and he catalyst's surface, with a lower thickness of the diffusive boundary layer during the hydrodynamic measurements. On the other hand, the onset potential is lower than typical LSV curves for Pt/C that generally starts showing catalytic activity from 1V. For the same reason, from the Tafel plot in **Figure 6b**, the i_0 correspondent to the intercept of the curve is around $1*10^{-8}$ A cm^{-2} (compared to a value of around $2.8*10^{-7}$ for a Pt/C). On the other hand, the Tafel slope, taken from the linear region of the IR-corrected voltage curve reveals a value as low as 68 mV $dec.^{-1}$. To exclude the possibility that the loss can be attributed to a non-optimal reaction pathway, the number of electrons exchanged is estimated using the Koutecky-Levich equation [65]:

$$\frac{1}{i} = \frac{1}{B}\,\omega^{-\frac{1}{2}} + \frac{1}{i_k}$$

with

$$B = 0.62\,nF\,C_{O_2}\,D_{O_2}^{\frac{2}{3}}\,\nu^{-\frac{1}{6}}$$

Where B= 2345 $cm^2\,A^{-1}\,rad^{1/2}$ and i_k = 576 mA cm^{-2} can be obtained from the fitting shown in **Figure 6c**. For a 0.5M H_2SO_4 solution[66] D_{O2} = 2.1*10-5 cm^2s^{-1}, C_{O2} = $1.03*10^{-6}$ mol cm^{-3} and ν = 0.0107 cm^2s^{-1}, a value of 4.2 is found for n, confirming the four-electron pathway. Moreover, the

ring current was monitored during the measurements, showed no significant signal when the ring potential was kept at constant 1V to oxidize the formed peroxide intermediates (**Figure SI2**).

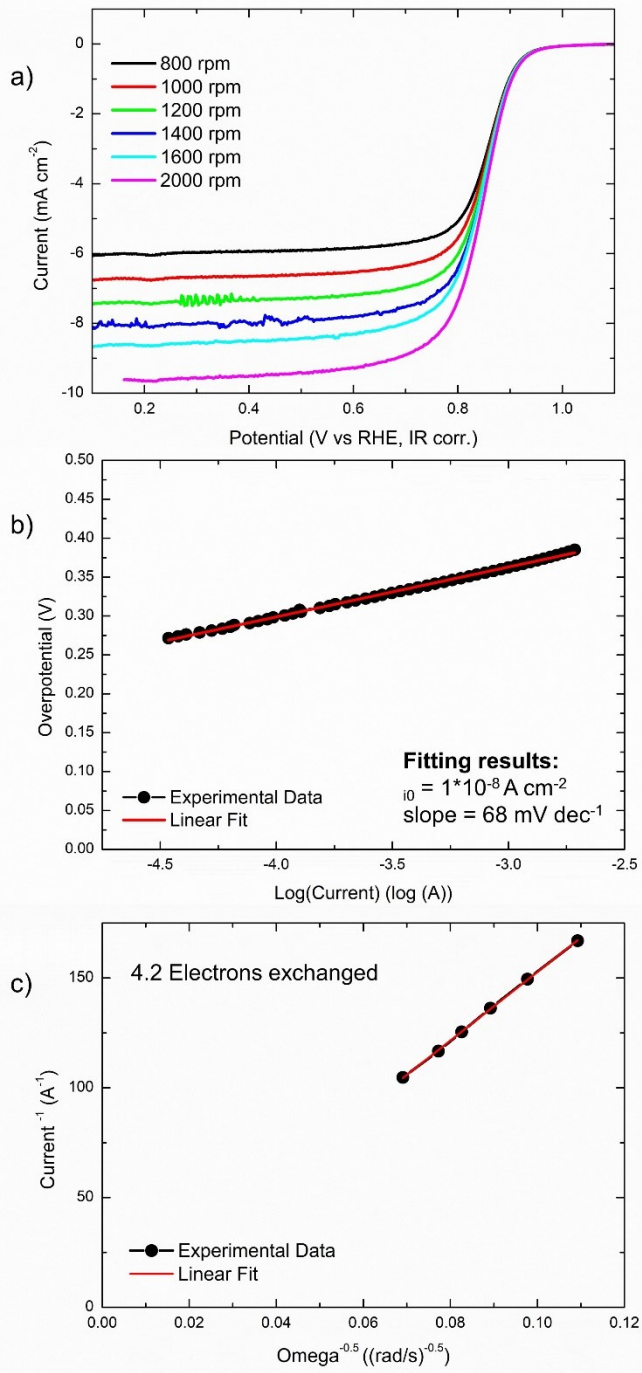

Figure 6. a) Linear sweep voltammetries in RRDE setup, 0.1M $HClO_4$, 0.005 Vs^{-1} scan rate. b) Tafel plot of the 1600 rpm LSV curve. c) Levich plot for the Pt/TiN. Each point is the average current between three points, taken respectively at 0.2, 0.4 and 0.6V

This suggests a reaction pathway that is mainly characterized by a four-electron transfer, that is preferable for ORR in acidic media[67]. Our hypothesis for this behavior relies on the high oxygen

content in the film (**Figure 2c**): the presence of amorphous TiO_2 can hinder the catalytic activity since a semiconductor – metal or a semiconductor – electrolyte interface can cause a net activation loss due to a less efficient charge transfer. Moreover, there could be an effect of the low particle size on the electrical conductivity of the TiN network, as highlighted by Shin et al[23]. Nevertheless, the low slope obtained in the linear sweep voltammetry holds promises for further improvement in the performances: by reducing the oxygen content and at the same time increasing the crystal fraction and size of the HTNTF it should be possible to overcome the net potential loss introduced, and achieve better current densities, comparable with more conductive carbonaceous supports.

3.3 MEA testing

In the development of a fuel cell catalyst, actual fuel cell testing must be part of the process, to integrate the final catalyst design and optimize it in actual PEMFC hardware. In order to fabricate an electrode for MEA application, we chose the ALD process, that is able to coat conformally the complex morphology of the HTNTF. In this case, the electrodeposition is not a viable option, due to several factors: (i) it is difficult to scale up the pulsed electrodeposition process to a lab scale MEA while granting uniformity of the platinum electrodeposited over the area and (ii) the eletrodeposition process is not compatible with the modified decal method shown in Section 2.4, since the flat silicon substrate and the sacrificial MoOx layer are not electrically conductive. We set a loading of 0.360 mg cm^{-2}, to maintain similarity with the previous catalyst obtained by electrodeposition on the RRDE tip.

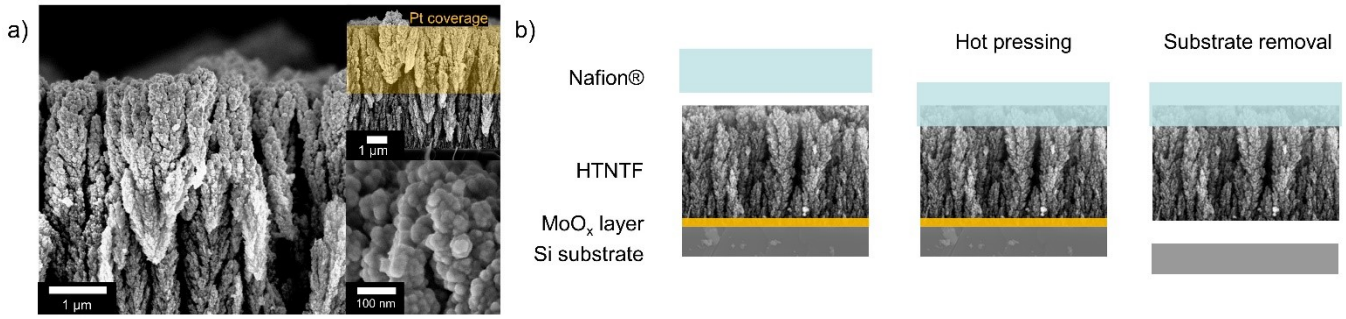

Figure 7 a) SEM images of the platinum by ALD deposited on 5 µm HTNTF. In the inset is shown the Pt coverage over the film thickness (upper picture) and a detail of the precise coverage over the complex morphology of the HTNTF. c) schematic of the decal method for the HTNTF transfer on the Nafion ® membrane

Active area is calculated from the hydrogen desorption peaks in the low potential region of the CV (**Figure 8d**). The cathodic contribution of hydrogen evolution in the total charge from the previous sweep has been subtracted to the total charge value. A value of 42.3 m^2g^{-1} is calculated due to the high surface area that the nanotrees expose for the Pt coating, although the coverage, as seen from SEM images, **Figure 7b**, is only 2.5 µm over a total thickness of 5µm. XRD analysis is performed on the Pt by ALD (**Figure SI3**), the cell parameter is 3.919 Å, with a compressive strain of the cubic lattice of only 0.08%, meaning that the material, with respect to electrodeposited platinum, is less subject to stress during deposition. Mean crystalline domains is 11.7 nm. The polarization curve, **Figure 8a,** is characterized by a high OCV (> 0.9 V) and rather high ohmic resistance. The maximum power density achieved is 0.1 W cm^{-1} (**Figure 8b**), obtained at 0.3 V.

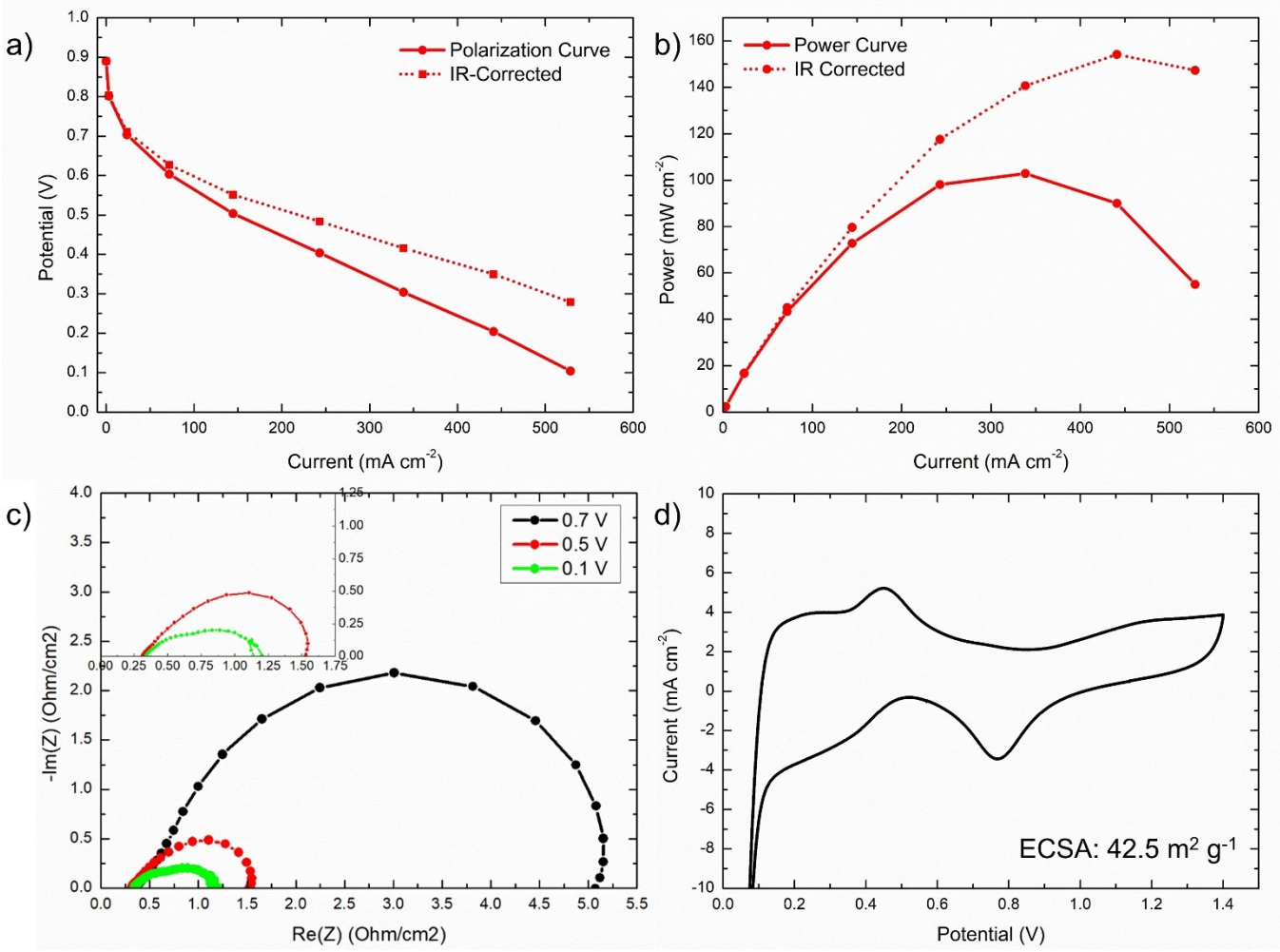

Figure 8. a) Polarization curve of the MEA performed at 80°C, 90% RH on both sides and 100kPa back pressure. The dotted line corresponds to the IR corrected curve. b) Power curve of the MEA. c) EIS performed at different voltage values. d) Cyclic voltammetry of the cell performed at 80°C, H_2/N_2 gases, 100% RH on both side and no back pressure

In order to understand the cell behavior better, EIS spectra were performed at 0.7 V, 0.5 V and 0.1 V (**Figure 8c**). The values of the high frequency resistance (HFR) values reported are as high as 0.3 Ω cm^{-2}. Moreover, a considerable linear branch at high frequency is registered, which is generally associated with the presence of proton transport resistance inside the electrode[68], similar to dehydration. This suggests that the Nafion® coverage is not yet optimal. No oxygen transport feature is registered in the spectrum in the low frequency region[69] as no oxygen transport limitation is visible in the polarization curve, so the reactant diffusion is able to sustain current densities as

high as 0.5 A cm^{-2} without limitations. Therefore, the predominant semicircular features can be attributed to the ORR charge transfer process in all the spectra, as confirmed by the related frequencies typical of such reaction[70]. By investigating the charge transfer semicircle, some considerations can be done about the reaction mechanism. Using the following formula:

$$R_{CT} = \frac{b}{i} = \frac{RT}{i\,\alpha\,F}$$

Where RCT is the charge transfer resistance, taken as double of the maximum in the imaginary part of the impedance, b the Tafel Slope, i the specific current taken from the polarization, and α the charge transfer coefficient[71]. For typical ORR reaction in a fuel cell α is 0.5 and therefore b is 0.061 V. The slopes for our cell are 0.102 V dec^{-1}, 0.140 V dec^{-1}, 0.212 V dec^{-1} at 0.7 V, 0.5 V and 0.1 V, respectively. These higher values of the slope can be attributed to a modification of the dominant reaction mechanism and to a limiting proton transport, since the α coefficient is also different. We attribute this behavior, similarly to the RDE case, to the oxidation of the catalyst support and the interaction of platinum with semiconducting titanium monoxide. Further improvements are necessary together with the HTNTF morphology and composition tuning, accounting for the resistive behavior, that is noticeable in the low potential region, as a reflection of the high HFR registered in the EIS spectra, according to[23]. The optimization of the Pt coverage through a fine tuning of the ALD process is also necessary to achieve monolayer/sub-monolayer coverage, being able to meet rate of consumption of the Pt resource that are sustainable for the mass production. Nafion® loading and dispersion must be optimized as well, to have better coverage of the nanostructure and therefore improving the proton transport.

4. Conclusions and perspectives

In this work, a novel approach to the fabrication of hierarchical TiN nanostructure thin-film electrodes is presented. The flexibility of the PL-SBD process allows to easily reach the characteristic morphology, such as porous nanotrees required for optimal catalyst layer morphology for PEMFCs. The tree-like HTNs were obtained and decorated with the active platinum electrocatalyst and showed exceptional stability with an ECSA loss after 15000 cycles of only 13%, compared to the >50% loss for carbonaceous materials after 5000 cycles. We have also demonstrated the electrode to be functional within an actual MEA: a Pt/TiN catalyst layer was fabricated by means of ALD on the TiN films and transferred onto a Nafion membrane through a modified decal method, developed for our application. The proof-of-concept cell has shown substantial power densities and high ECSA values, demonstrating that the novel fabrication method holds significant promise for future MEA optimization and scale-up. If we can replicate the same stability obtained in the RDE setup, an increase of the device lifetime of the entire fuel cell can be achieved.

5. Acknowledgements

D. C. Sabarirajan and I.V. Zenyuk acknowledge support from National Science Foundation under Grant No. 1652445. V. Dal Santo and F. Bossola acknowledge financial support from EIT Raw Materials through project FREECATS (Project no. 15054).

6. References

(1) Service, R. F. Shrinking Fuel Cells Promise Power in Your Pocket. *Science (80-.).* **2002**,

296 (5571), 1222–1224. https://doi.org/10.1126/science.296.5571.1222.

(2) Groger, O.; Gasteiger, H. A.; Suchsland, J. Review — Electromobility : Batteries or Fuel Cells ? **2015**, *162* (14). https://doi.org/10.1149/2.0211514jes.

(3) Eberle, U.; Müller, B.; von Helmolt, R. Fuel Cell Electric Vehicles and Hydrogen Infrastructure: Status 2012. *Energy Environ. Sci.* **2012**, *5* (10), 8780. https://doi.org/10.1039/c2ee22596d.

(4) Borup, R.; Meyers, J.; Pivovar, B.; Kim, Y. S.; Mukundan, R.; Garland, N.; Myers, D.; Wilson, M.; Garzon, F.; Wood, D.; et al. Scientific Aspects of Polymer Electrolyte Fuel Cell Durability and Degradation. *Chem. Rev.* **2007**, *107* (10), 3904–3951. https://doi.org/10.1021/cr0501821.

(5) Castanheira, L.; Dubau, L.; Mermoux, M.; Berthomé, G.; Caqué, N.; Rossinot, E.; Chatenet, M.; Maillard, F. Carbon Corrosion in Proton-Exchange Membrane Fuel Cells. *From Model Exp. to Real-Life Oper. Membr. Electrode Assem.* **2014**, *4* (7), 2258–2267. https://doi.org/10.1021/cs500449q M4 - Citavi.

(6) He, D.; Mu, S.; Pan, M. Perfluorosulfonic Acid-Functionalized Pt/Carbon Nanotube Catalysts with Enhanced Stability and Performance for Use in Proton Exchange Membrane

Fuel Cells. *Carbon N. Y.* **2011**, *49* (1), 82–88. https://doi.org/10.1016/j.carbon.2010.08.045.

(7) Chung, H. T.; Won, J. H.; Zelenay, P. Active and Stable Carbon Nanotube/Nanoparticle Composite Electrocatalyst for Oxygen Reduction. *Nat. Commun.* **2013**, *4* (May), 1922. https://doi.org/10.1038/ncomms2944.

(8) Seger, B.; Kamat, P. V. Electrocatalytically Active Graphene-Platinum Nanocomposites. Role of 2-D Carbon Support in Pem Fuel Cells. *J. Phys. Chem. C* **2009**, *113*, 7990–7995. https://doi.org/10.1021/jp900360k.

(9) Soo, L. T.; Loh, K. S.; Mohamad, A. B.; Daud, W. R. W.; Wong, W. Y. An Overview of the Electrochemical Performance of Modified Graphene Used as an Electrocatalyst and as a Catalyst Support in Fuel Cells. *Appl. Catal. A Gen.* **2015**, *497*, 198–210. https://doi.org/10.1016/j.apcata.2015.03.008.

(10) Higgins, D.; Zamani, P.; Yu, A.; Chen, Z. The Application of Graphene and Its Composites in Oxygen Reduction Electrocatalysis: A Perspective and Review of Recent Progress. *Energy Environ. Sci.* **2016**, *9* (2), 357–390. https://doi.org/10.1039/C5EE02474A.

(11) Zhang, Z.; Liu, J.; Gu, J.; Su, L.; Cheng, L. An Overview of Metal Oxide Materials as Electrocatalysts and Supports for Polymer Electrolyte Fuel Cells. *Energy Environ. Sci.*

2014, *7* (8), 2535–2558. https://doi.org/10.1039/C3EE43886D.

(12) Aryanpour, M.; Hoffmann, R.; Disalvo, F. J. Tungsten-Doped Titanium Dioxide in the Rutile Structure: Theoretical Considerations. *Chem. Mater.* **2009**, *21* (8), 1627–1635. https://doi.org/10.1021/cm900329k.

(13) Subban, C. V; Zhou, Q.; Hu, a; Moylan, T. E.; Wagner, F. T.; DiSalvo, F. J. Sol-Gel Synthesis, Electrochemical Characterization, and Stability Testing of Ti0.7W0.3O2 Nanoparticles for Catalyst Support Applications in Proton-Exchange Membrane Fuel Cells. *J. Am. Chem. Soc.* **2010**, *132*, 17531–17536. https://doi.org/10.1021/ja1074163.

(14) Abdullah, N.; Kamarudin, S. K. Titanium Dioxide in Fuel Cell Technology: An Overview. *J. Power Sources* **2015**, *278*, 109–118. https://doi.org/10.1016/j.jpowsour.2014.12.014.

(15) Fabbri, E.; Rabis, A.; Kötz, R.; Schmidt, T. J. Pt Nanoparticles Supported on Sb-Doped SnO 2 Porous Structures: Developments and Issues. *Phys. Chem. Chem. Phys.* **2014**, *16* (27), 13672–13681. https://doi.org/10.1039/C4CP00238E.

(16) Waldecker, P. I. J. Vapor Deposition Process for Engineering of Dispersed PEMFC ORR Pt / NbO x / C Catalysts. **2017**.

(17) Allmaier, H.; Chioncel, L.; Arrigoni, E. Titanium Nitride: A Correlated Metal at the Threshold of a Mott Transition. *Phys. Rev. B - Condens. Matter Mater. Phys.* **2009**, *79* (23), 1–7. https://doi.org/10.1103/PhysRevB.79.235126.

(18) Avasarala, B.; Haldar, P. On the Stability of TiN-Based Electrocatalysts for Fuel Cell Applications. *Int. J. Hydrogen Energy* **2011**, 1–10. https://doi.org/10.1016/j.ijhydene.2010.12.107.

(19) Yang, M.; Cui, Z.; DiSalvo, F. J. Mesoporous Titanium Nitride Supported Pt Nanoparticles as High Performance Catalysts for Methanol Electrooxidation. *Phys. Chem. Chem. Phys.* **2013**, *15* (4), 1088–1092. https://doi.org/10.1039/C2CP44215A.

(20) KAKINUMA, K.; WAKASUGI, Y.; UCHIDA, M.; KAMINO, T.; UCHIDA, H.; WATANABE, M. Electrochemical Activity and Durability of Platinum Catalysts Supported on Nanometer-Size Titanium Nitride Particles for Polymer Electrolyte Fuel Cells. *Electrochemistry* **2011**, *79* (5), 399–403. https://doi.org/10.5796/electrochemistry.79.399.

(21) Kim, H.; Cho, M. K.; Kwon, J. A.; Jeong, Y. H.; Lee, K. J.; Kim, N. Y.; Kim, M. J.; Yoo, S. J.; Jang, J. H.; Kim, H.-J.; et al. Highly Efficient and Durable TiN Nanofiber Electrocatalyst Supports. *Nanoscale* **2015**, *7* (44), 18429–18434.

https://doi.org/10.1039/C5NR04082E.

(22) Pan, Z.; Xiao, Y.; Fu, Z.; Zhan, G.; Wu, S.; Xiao, C.; Hu, G.; Wei, Z. Hollow and Porous Titanium Nitride Nanotubes as High-Performance Catalyst Supports for Oxygen Reduction Reaction. *J. Mater. Chem. A* **2014**, *2* (34), 13966. https://doi.org/10.1039/C4TA02402H.

(23) Shin, H.; Kim, H. Il; Chung, D. Y.; Yoo, J. M.; Weon, S.; Choi, W.; Sung, Y. E. Scaffold-like Titanium Nitride Nanotubes with a Highly Conductive Porous Architecture as a Nanoparticle Catalyst Support for Oxygen Reduction. *ACS Catal.* **2016**, *6* (6), 3914–3920. https://doi.org/10.1021/acscatal.6b00384.

(24) Zheng, Y.; Zhang, J.; Zhan, H.; Sun, D.; Dang, D.; Tian, X. L. Porous and Three Dimensional Titanium Nitride Supported Platinum as an Electrocatalyst for Oxygen Reduction Reaction. *Electrochem. commun.* **2018**, *91* (May), 31–35. https://doi.org/10.1016/j.elecom.2018.04.021.

(25) Kwon, J. A.; Kim, M. S.; Shin, D. Y.; Kim, J. Y.; Lim, D. H. First-Principles Understanding of Durable Titanium Nitride (TiN) Electrocatalyst Supports. *J. Ind. Eng. Chem.* **2017**, *49*, 69–75. https://doi.org/10.1016/j.jiec.2017.01.008.

(26) DOE working group 10/04/2011. Rotating Disk Electrode Aqueous Electrolyte Accelerated

Stress Tests for PGM Electrocatalyst/Support Durability Evaluation https://www.energy.gov/eere/fuelcells/downloads/rotating-disk-electrode-aqueous-electrolyte-accelerated-stress-tests-pgm.

(27) Garland, N.; Benjamin, T.; Kopasz, J. DOE Fuel Cell Program: Durability Technical Targets and Testing Protocols. *ECS Trans.* **2007**, *11* (1), 923–931. https://doi.org/10.1149/1.2781004.

(28) Vliet, D. F. Van Der; Wang, C.; Tripkovic, D.; Strmcnik, D.; Zhang, X. F.; Debe, M. K.; Atanasoski, R. T.; Markovic, N. M.; Stamenkovic, V. R. Mesostructured Thin Films as Electrocatalysts with Tunable Composition and Surface Morphology. *Nat. Mater.* **2012**, *11* (11), 1–8. https://doi.org/10.1038/nmat3457.

(29) Steinbach, A. J.; Noda, K.; Debe, M. K. Stop-Start and High-Current Durability Testing of Nanostructured Thin Film Catalysts for PEM Fuel Cells. *ECS Trans.* **2006**, *3* (1), 835–853.

(30) Debe, M. K. Electrocatalyst Approaches and Challenges for Automotive Fuel Cells. *Nature* **2012**, *486* (7401), 43–51. https://doi.org/10.1038/nature11115.

(31) Steinbach, A. J.; Allen, J. S.; Borup, R. L.; Hussey, D. S.; Jacobson, D. L.; Komlev, A.; Kwong, A.; MacDonald, J.; Mukundan, R.; Pejsa, M. J.; et al. Anode-Design Strategies for

Improved Performance of Polymer-Electrolyte Fuel Cells with Ultra-Thin Electrodes. *Joule* **2018**, 1–16. https://doi.org/10.1016/j.joule.2018.03.022.

(32) Zenyuk, I. V.; Das, P. K.; Weber, A. Z. Understanding Impacts of Catalyst-Layer Thickness on Fuel-Cell Performance via Mathematical Modeling. *J. Electrochem. Soc.* **2016**, *163* (7), F691–F703. https://doi.org/10.1149/2.1161607jes.

(33) Department of Energy, U. U.S. Department of Energy Hydrogen and Fuel Cells Program 2015 Annual Merit Review (AMR) and Peer Evaluation Report: Fuel Cells. **2015**, 185–341. https://doi.org/DOE/GO-102015-4730.

(34) Liu, S.; Pan, G. L.; Li, G. R.; Gao, X. P. Copper Hexacyanoferrate Nanoparticles as Cathode Material for Aqueous Al-Ion Batteries. *J. Mater. Chem. A* **2015**, *3* (3), 959–962. https://doi.org/10.1039/c4ta04644g.

(35) Passoni, L.; Ghods, F.; Docampo, P.; Abrusci, A.; Martí-Rujas, J.; Ghidelli, M.; Divitini, G.; Ducati, C.; Binda, M.; Guarnera, S.; et al. Hyperbranched Quasi-1d Nanostructures for Solid-State Dye-Sensitized Solar Cells. *ACS Nano* **2013**, *7* (11), 10023–10031. https://doi.org/10.1021/nn403979h.

(36) Biserni, E.; Garino, N.; Li Bassi, A.; Bruno, P.; Gerbaldi, C. Mesoporous Silicon

Nanostructures by Pulsed Laser Deposition as Li-Ion Battery Anodes. *ECS Trans.* **2014**, *62* (1), 107–115. https://doi.org/10.1149/06201.0107ecst.

(37) Di Fonzo, F.; Tonini, D.; Li Bassi, A.; Casari, C. S.; Beghi, M. G.; Bottani, C. E.; Gastaldi, D.; Vena, P.; Contro, R. Growth Regimes in Pulsed Laser Deposition of Aluminum Oxide Films. *Appl. Phys. A Mater. Sci. Process.* **2008**, *93* (3), 765–769. https://doi.org/10.1007/s00339-008-4720-y.

(38) Ghadirzadeh, A.; Fumagalli, F.; Mezzetti, A.; Bellani, S.; Meda, L.; Antognazza, M. R.; Di Fonzo, F. A Three-Dimensional Architecture for Hydrogen-Evolving, Host/Guest, Hybrid Organic/Inorganic Photocathodes Based on Nanolamellar MoO_3 Scaffolds. *ChemPhotoChem* **2018**, *2* (3), 283–292. https://doi.org/10.1002/cptc.201700159.

(39) Mazzolini, P.; Acartürk, T.; Chrastina, D.; Starke, U.; Casari, C. S.; Gregori, G.; Bassi, A. L. Controlling the Electrical Properties of Undoped and Ta-Doped TiO2polycrystalline Films via Ultra-Fast-Annealing Treatments. *Adv. Electron. Mater.* **2016**, *2* (3), 1–9. https://doi.org/10.1002/aelm.201500316.

(40) Nava, G.; Fumagalli, F.; Neutzner, S.; Fonzo, F. Di. Large Area Porous 1D Photonic Crystals Comprising Silicon Hierarchical Nanostructures Grown by Plasma-Assisted , Nanoparticle Jet Deposition. **2018**.

(41) Trifiletti, V.; Ruffo, R.; Turrini, C.; Tassetti, D.; Brescia, R.; Di Fonzo, F.; Riccardi, C.; Abbotto, A. Dye-Sensitized Solar Cells Containing Plasma Jet Deposited Hierarchically Nanostructured TiO2thin Photoanodes. *J. Mater. Chem. A* **2013**, *1* (38), 11665–11673. https://doi.org/10.1039/c3ta11485f.

(42) Biganzoli, I.; Fumagalli, F.; Fonzo, F. Di; Barni, R.; Riccardi, C. A Supersonic Plasma Jet Source for Controlled and Efficient Thin Film Deposition. *J. Mod. Phys.* **2012**, *2012* (October), 1626–1638. https://doi.org/10.4236/jmp.2012.330200.

(43) Schramke, K. S.; Qin, Y.; Held, J. T.; Mkhoyan, K. A.; Kortshagen, U. R. Nonthermal Plasma Synthesis of Titanium Nitride Nanocrystals with Plasmon Resonances at Near-Infrared Wavelengths Relevant to Photothermal Therapy. *ACS Appl. Nano Mater.* **2018**, *1* (6), 2869–2876. https://doi.org/10.1021/acsanm.8b00505.

(44) Alvarez Barragan, A.; Ilawe, N. V; Zhong, L.; Wong, B. M.; Mangolini, L. A Non-Thermal Plasma Route to Plasmonic TiN Nanoparticles. *J. Phys. Chem. C* **2017**, *121* (4), 2316–2322. https://doi.org/10.1021/acs.jpcc.6b08910.

(45) Geohegan, D. B.; Puretzky, A. A. Dynamics of Laser Ablation Plume Penetration through Low Pressure Background Gases. *Appl. Phys. Lett.* **1995**, *67* (1995), 197. https://doi.org/10.1063/1.114665.

(46) Balandeh, M.; Mezzetti, A.; Tacca, A.; Leonardi, S.; Marra, G.; Divitini, G.; Ducati, C.; Meda, L.; Di Fonzo, F. Quasi-1D Hyperbranched WO<inf>3</Inf> Nanostructures for Low-Voltage Photoelectrochemical Water Splitting. *J. Mater. Chem. A* **2015**, *3* (11), 6110–6117. https://doi.org/10.1039/c4ta06786j.

(47) Passoni, L.; Bonvini, G.; Luzio, A.; Facibeni, A.; Bottani, C. E.; Di Fonzo, F. Multiscale Effect of Hierarchical Self-Assembled Nanostructures on Superhydrophobic Surface. *Langmuir* **2014**, *30* (45), 13581–13587. https://doi.org/10.1021/la503410m.

(48) Yarlagadda, V.; Carpenter, M. K.; Moylan, T. E.; Kukreja, R. S.; Koestner, R.; Gu, W.; Thompson, L.; Kongkanand, A. Boosting Fuel Cell Performance with Accessible Carbon Mesopores. *ACS Energy Lett.* **2018**, 618–621. https://doi.org/10.1021/acsenergylett.8b00186.

(49) Park, Y. C.; Tokiwa, H.; Kakinuma, K.; Watanabe, M.; Uchida, M. Effects of Carbon Supports on Pt Distribution, Ionomer Coverage and Cathode Performance for Polymer Electrolyte Fuel Cells. *J. Power Sources* **2016**, *315*, 179–191. https://doi.org/10.1016/j.jpowsour.2016.02.091.

(50) Morozov, I. G.; Belousova, O. V.; Belyakov, O. A.; Parkin, I. P.; Sathasivam, S.; Kuznetcov, M. V. Titanium Nitride Room-Temperature Ferromagnetic Nanoparticles. *J.*

Alloys Compd. **2016**, *675* (March), 266–276. https://doi.org/10.1016/j.jallcom.2016.03.111.

(51) Spengler, W.; Kaiser, R.; Bilz, H. RESONANT RAMAN SCATTERING IN A SUPERCONDUCTING TRANSITION METAL COMPOUND - TiN*. *Solid State Commun.* **1975**, *17*, 19–22. https://doi.org/10.1016/0038-1098(75)90325-7.

(52) Avasarala, B.; Haldar, P. Electrochimica Acta Electrochemical Oxidation Behavior of Titanium Nitride Based Electrocatalysts under PEM Fuel Cell Conditions. *Electrochim. Acta* **2010**, *55* (28), 9024–9034. https://doi.org/10.1016/j.electacta.2010.08.035.

(53) Cheng, Y. H.; Tay, B. K.; Lau, S. P.; Kupfer, H.; Richter, F. Substrate Bias Dependence of Raman Spectra for TiN Films Deposited by Filtered Cathodic Vacuum Arc. *J. Appl. Phys.* **2002**, *92* (4), 1845–1849. https://doi.org/10.1063/1.1491588.

(54) Spengler, W.; Kaiser, R.; Christensen, A. N.; Müller-Vogt, G. Raman Scattering, Superconductivity, and Phonon Density of States of Stoichiometric and Nonstoichiometric TiN. *Phys. Rev. B* **1978**, *17* (3), 1095–1101. https://doi.org/10.1103/PhysRevB.17.1095.

(55) Chichagov, A. V. et al. Information-Calculating System on Crystal Structure Data of Minerals. *Kristallographiya* **1990**, *35* (3), 610–616.

(56) Murray, J. L.; Wriedt, H. A. The O-Ti (Oxygen-Titanium) System. *Bull. Alloy Phase Diagr.* **1987**, *8*, 148–165.

(57) Kim, W.; Park, J.; Suh, C.; Cho, S.; Lee, S.; Shon, I.-J. Synthesis of TiN Nanoparticles by Explosion of Ti Wire in Nitrogen Gas. *Mater. Trans.* **2009**, *50* (12), 2897–2899. https://doi.org/10.2320/matertrans.M2009297.

(58) Morozov, I. G.; Belousova, O. V; Belyakov, O. A.; Parkin, I. P.; Sathasivam, S.; Kuznetcov, M. V. Titanium Nitride Room-Temperature Ferromagnetic Nanoparticles. *J. Alloys Compd.* **2016**, *675*, 266–276. https://doi.org/10.1016/j.jallcom.2016.03.111.

(59) Avasarala, B.; Haldar, P. Electrochemical Oxidation Behavior of Titanium Nitride Based Electrocatalysts under PEM Fuel Cell Conditions. *Electrochim. Acta* **2010**, *55* (28), 9024–9034. https://doi.org/10.1016/j.electacta.2010.08.035.

(60) Bard, A. J.; Faulkner, L. R. *Electrochemical Methods : Fundamentals and Applications*; 2001.

(61) Du, M.; Cui, L.; Cao, Y.; Bard, A. J. Mechanoelectrochemical Catalysis of the Effect of Elastic Strain on a Platinum Nanofilm for the ORR Exerted by a Shape Memory Alloy Substrate. *J. Am. Chem. Soc.* **2015**, *137* (23), 7397–7403.

https://doi.org/10.1021/jacs.5b03034.

(62) Yang, Y.; Kumar, K. S. Elastic Strain Effects on the Catalytic Response of Pt and Pd Thin Films Deposited on Pd–Zr Metallic Glass. *J. Mater. Res.* **2017**, *32* (14), 2690–2699. https://doi.org/10.1557/jmr.2017.169.

(63) Department of Energy, U. Fuel Cell Tech Team Accelerated Stress Test and Polarization Curve Protocols for PEM Fuel Cells https://energy.gov/sites/prod/files/2015/08/f25/fcto_dwg_usdrive_fctt_accelerated_stress_tests_jan2013.pdf.

(64) Castanheira, L.; Silva, W. O.; Lima, F. H. B.; Crisci, A.; Dubau, L.; Maillard, F. Carbon Corrosion in Proton-Exchange Membrane Fuel Cells: Effect of the Carbon Structure, the Degradation Protocol, and the Gas Atmosphere. *ACS Catal.* **2015**, *5* (4), 2184–2194. https://doi.org/10.1021/cs501973j.

(65) Huang, X.; Dai, B.; Ren, Y.; Xu, J.; Zhu, P. Preparation and Study of Electromagnetic Interference Shielding Materials Comprised of Ni-Co Coated on Web-like Biocarbon Nanofibers via Electroless Deposition. *J. Nanomater.* **2015**, *2015*. https://doi.org/10.1155/2015/320306.

(66) Seifitokaldani, A.; Savadogo, O. Electrochemically Stable Titanium Oxy-Nitride Support for Platinum Electro-Catalyst for PEM Fuel Cell Applications. *Electrochim. Acta* **2015**, *167*, 237–245. https://doi.org/10.1016/j.electacta.2015.03.189.

(67) Ramaswamy, N.; Mukerjee, S. Fundamental Mechanistic Understanding of Electrocatalysis of Oxygen Reduction on Pt and Non-Pt Surfaces: Acid versus Alkaline Media. *Adv. Phys. Chem.* **2012**, *2012*. https://doi.org/10.1155/2012/491604.

(68) Baricci, A.; Zago, M.; Casalegno, A. A Quasi 2D Model of a High Temperature Polymer Fuel Cell for the Interpretation of Impedance Spectra. *Fuel Cells* **2014**, *14* (6), 926–937. https://doi.org/10.1002/fuce.201300147.

(69) Baricci, A.; Mereu, R.; Messaggi, M.; Zago, M.; Inzoli, F.; Casalegno, A. Application of Computational Fluid Dynamics to the Analysis of Geometrical Features in PEM Fuel Cells Flow Fields with the Aid of Impedance Spectroscopy. *Appl. Energy* **2017**, *205* (August), 670–682. https://doi.org/10.1016/j.apenergy.2017.08.017.

(70) Baricci, A.; Zago, M.; Casalegno, A. Modelling Analysis of Heterogeneity of Ageing in High Temperature Polymer Electrolyte Fuel Cells: Insight into the Evolution of Electrochemical Impedance Spectra. *Electrochim. Acta* **2016**, *222*, 596–607. https://doi.org/10.1016/j.electacta.2016.11.014.

(71) Kulikovsky, A. *Analytical Modelling of Fuel Cells*; Elsevier B.V., 2010.

SUPPORTING INFORMATION

SI 1. Platinum XRD

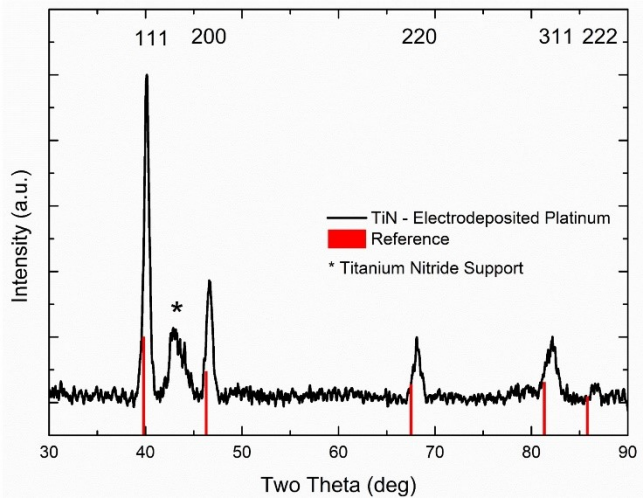

Figure SI 1. XRD pattern of the TiN/Pt catalyst with the reference from[55]

SI 2. Ring Current

No relevant ring current was measured at the platinum ring kept at 1V during LSV measurements

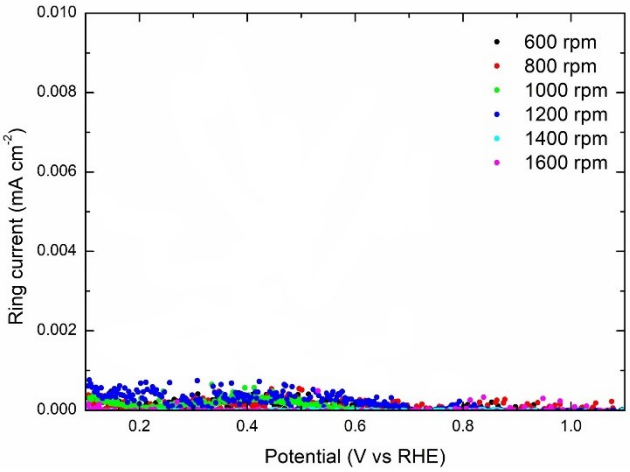

Figure SI 2~~3~~. Current monitored during LSV of Pt/TiN catalyst on the ring f the RRDE. The potential of the Pt ring was kept at 1V constant during the measurements. Measurement was performed in 0.1 M $HClO_4$

SI 3. ALD platinum XRD pattern

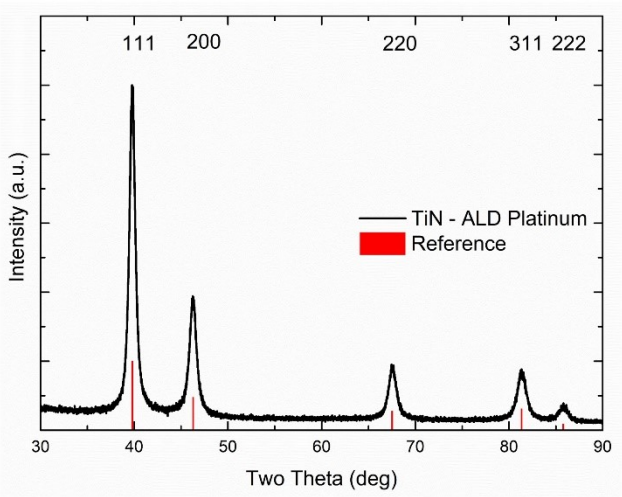

Figure SI 34. XRD pattern of the ALD deposited Pt on HTNTF, with reference to[55]